



Statics and dynamics of a finite two-dimensional colloidal system with competing attractive critical Casimir and repulsive magnetic dipole interactions

Kevin Marolt * and Roland Roth *Institute for Theoretical Physics, University of Tübingen, Auf der Morgenstelle 14, 72076 Tübingen, Germany*

(Received 9 July 2020; accepted 22 September 2020; published 13 October 2020)

We continue our theoretical study of a recently proposed two-dimensional colloidal system with attractive critical Casimir and repulsive magnetic dipole forces that can be tuned easily and independently from each other via the temperature and the strength of an external magnetic field, respectively [K. Marolt, M. Zimmermann, and R. Roth, *Phys. Rev. E* **100**, 052602 (2019)]. Using this freedom, it is possible to construct a competing interaction potential that causes microphase separation featuring spatially inhomogeneous cluster, stripe, and bubble phases in the bulk, i.e., in an infinite system without an external potential. In the present work, we demonstrate by means of density functional theory that microphase separation can also occur in finite geometries. In a square cell with a side length of 20 or 30 colloid diameters, we observe the emergence of highly structured cluster and ring phases at intermediate bulk densities in addition to almost uniform fluid phases for lower and higher bulk densities. We then employ dynamic density functional theory to determine how the system reacts when the temperature and the magnetic field are altered over time, and we show how to induce a transition from the liquid to the cluster/ring phase and also from the cluster directly to the ring phase. We find that often a slowly varying and nontrivial path in parameter space is required to reach a stable state, whereas abrupt changes are prone to lead to metastable configurations.

DOI: [10.1103/PhysRevE.102.042608](https://doi.org/10.1103/PhysRevE.102.042608)

I. INTRODUCTION

Under the right circumstances, certain soft matter systems are known to exhibit stable density profiles with curious inhomogeneities [1]. Remarkably, this so-called microphase separation can also be observed if the external potential is spatially uniform and, therefore, has to be primarily a consequence of the interparticle forces. In the case of diblock copolymers comprising two immiscible species of monomers, for example, the dependence of these forces on the molecules' orientation leads, at sufficiently low temperatures, to the formation of domains rich in either one or the other monomer type [2,3]. However, even isotropic interactions can be the cause of density modulations, as demonstrated by monolayers of amphiphilic molecules, such as phospholipids, at a flat air/water interface [4,5]. The amphiphiles align themselves roughly perpendicular to the interface: Their polar, hydrophilic head is drawn toward the water, whereas their apolar, hydrophobic tail is exposed to the air. While the tails attract each other over short distances due to van der Waals forces, the heads' dipoles repel one another even across larger separations. Although these interactions are radially symmetric within the monolayer, the competition between them can induce the development of microphases [6]: When balanced just right, the short-ranged attraction promotes local agglomerations of molecules that are, in their entirety, driven apart by the long-ranged repulsion.

Such self-assembling systems possess very similar phase diagrams [7–9], and, as shown by Ciach *et al.*, share a universal sequence of microphases for increasing bulk densities [10,11], irrespective of the details of the interaction among the constituent particles. In (effectively) two-dimensional systems, the three structures that usually emerge are clusters, stripes and bubbles. In an infinitely large system, theory predicts the thermodynamically stable configurations to be highly symmetrical insofar that clusters and bubbles are circular, equal in size and arranged in a hexagonal pattern, and that stripes are straight and parallel [12]. In experiments, however, this symmetry is always broken to some degree [13]; for instance, one may encounter haphazardly scattered clusters of different shapes and sizes, or stripes that bend and form labyrinthine networks [14–16].

Of course, some defects are inevitable since conditions are never completely ideal in an experiment; but it seems questionable whether excessively irregular patterns are even anywhere close to the true thermodynamic equilibrium. One might therefore ask which factors increase the likelihood of reaching a metastable state. We suspect that nonequilibrium dynamics, and specifically the manner in which the system is brought into the microphase regime, play a pivotal role. This would be in line with a report by Helm and Möhwald that, in a phospholipid monolayer, a rapid transition into the cluster phase through a fast compression leads to a much higher dispersity of cluster sizes than a slower one [17].

We wanted to carry out further investigations into this matter using a two-dimensional colloidal system with attractive critical Casimir and repulsive magnetic dipole forces that we have recently proposed and begun to study theoretically, and

*kevin.marolt@uni-tuebingen.de

that we expect to be also accessible to experiments [18]. The notable feature of this setup is that the strengths of attraction and repulsion can be adjusted independently from each other by simply altering two extrinsically controllable parameters: The temperature and an external magnetic field, respectively. The results of our density functional theory (DFT) calculations for an unbounded system have demonstrated that, given the correct tuning of these parameters, this system undergoes microphase separation offering the typical clusters, stripes and bubbles.

Now, for the present study, we were particularly interested in the time evolution of the density profile as a response to abrupt or gradual changes of the temperature and the magnetic field. In the hope of gaining new insights into the aforementioned difficulties of producing regular structures in experiments, we wanted to ascertain whether it would be possible to guide the system from one stable state to another in this way, and whether the fact that we have two independent parameters to tinker with would give us an advantage.

We chose to employ the framework of dynamic density functional theory (DDFT) for this task because it is a natural extension of DFT and allowed us to leverage most of the effort already put therein. Unfortunately, for infinite systems, one stumbles across a problem. In the static case, these can only be analyzed because the stable phases all have a periodic density profile, so that it is sufficient to consider only a single unit cell. However, the size of that unit cell depends on the parameters of the system, so that it becomes necessary to compare unit cells of different dimensions to find the true thermodynamic equilibrium. This implies that in the dynamical case, the volume (and perhaps even the shape) of the unit cell would potentially have to change over time to represent the real evolution of the system. Since we are not aware of any version of DDFT designed to accommodate this, we decided to restrict ourselves solely to bounded systems.

While this meant that we could not simply use our previous findings and jump directly into the dynamics, we thought it in and of itself worthwhile to study the effects of competing interactions in a finite geometry. On the one hand, because it by no means clear whether thermodynamically stable microphases exist at all in the presence of walls, and if so, what these might look like; on the other hand, because it should allow for more meaningful comparisons with experiments since these are subject to the same constraint.

We shall proceed as follows. In Sec. II, we first describe the general setup of our model system and the interactions between the particles. In Sec. III, we then explain how to analyze the static properties with DFT and present phase diagrams for square geometries of different sizes. Next, in Sec. IV, we give an overview of DDFT and demonstrate the dynamic behavior via the time evolution of the density profile for multiple scenarios, before finally drawing our conclusion in Sec. V.

II. SETUP

The experimental setup we aim to model essentially fuses that by Zvyagolskaya *et al.* [19,20] with the one by Bubeck *et al.* [21]. Spherical silica colloids with a paramagnetic core and a diameter a on the order of a few microns are submerged

in a binary mixture of water and 2,6-Lutidine. Under the force of gravity, they sediment toward the bottom of a confining glass cell with a rectangular base area $A = L_x \times L_y$ and form a flat monolayer (provided that they are sufficiently massive so that thermal fluctuations of their vertical position are negligible). The cell is placed on top of a heating element to control the temperature T and inside a homogeneous magnetic field with flux density B perpendicular to the monolayer.

The magnetic field induces the magnetic dipole moment $M = \chi_{\text{eff}} B$ in the colloids, where χ_{eff} is the effective magnetic susceptibility of their paramagnetic core. Between two colloids whose centers are a distance r apart, the dipole-dipole interaction leads to a long-ranged repulsion given by the potential

$$V_{\text{mag}}(r) = \frac{\mu_0 M^2}{4\pi r^3} = \frac{\mu_0 \chi_{\text{eff}}^2 B^2}{4\pi r^3}, \quad (1)$$

with the vacuum permeability μ_0 .

Through contact with the aqueous solvent, the surface of the silica colloids (and also that of the glass cell) acquire a negative charge [22]. This causes a screened electrostatic repulsion that weakens exponentially with the Debye screening length $\kappa^{-1} \ll a$, and can be effectively approximated as a hard core with diameter $d > a$ [19].

Because of their negative surface charge, the colloids also become hydrophilic and hence favor water over 2,6-Lutidine. Close to the critical demixing temperature T_c of the binary mixture, the confinement of the concentration fluctuations generates an attractive critical Casimir force between two adjacent colloids [23,24] that is described by the potential [19]

$$V_{\text{cas}}(r) = \frac{k_B T}{4} \frac{a}{r-a} \theta \left[\frac{r-a}{\xi(T)} \right], \quad (2)$$

where k_B is the Boltzmann constant and θ is the scaling function plotted in Fig. 1 [25,26]. The strength and range of V_{cas} depend predominantly on the mixture's bulk correlation length $\xi(T) = \xi_0 (|T - T_c|/T_c)^{-0.63}$ which diverges in the limit $T \rightarrow T_c$. In principle, colloids would become inseparably glued to each other as soon as their proper surfaces came into contact, since $V_{\text{cas}}(r) \rightarrow -\infty$ as $r \rightarrow a$; in practice, though, this is very unlikely because, as measurements show [23], the electrostatic repulsion beats the Casimir attraction

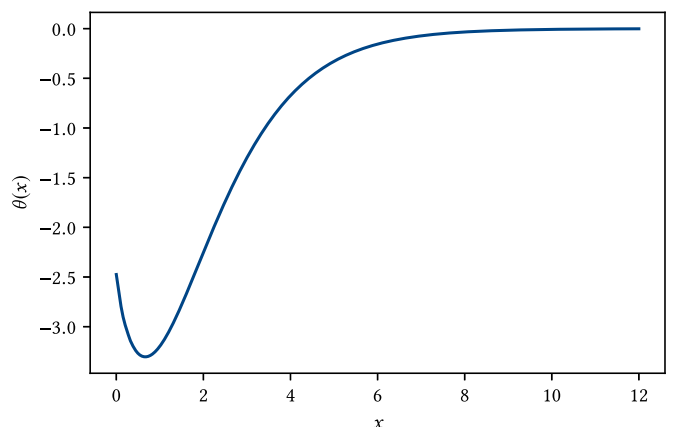


FIG. 1. The scaling function θ for the critical Casimir potential V_{cas} appearing in Eq. (2).

for very short particle separation. We note that the critical Casimir potential given in Eq. (2) is strictly speaking only valid for two isolated colloids. Due to their geometric origin, the critical Casimir forces are actually nonadditive and the interaction between three or more nearby colloids cannot be simply expressed as the pairwise sum of V_{cas} [27–29]. Dang *et al.* attribute discrepancies between the experimentally determined and theoretically predicted phase diagram of a colloidal system under the influence of critical Casimir forces to many-body effects [30], and Paladugu *et al.* were able to directly measure three-body critical Casimir forces [31]. While they are not irrelevant, many-body effects are unfortunately notoriously difficult to quantify and to incorporate because of their complicated dependence on the position, orientation and geometry of the interacting objects; even for the relatively simple case of three identical spherical colloids there does not yet exist a comprehensive description of the critical Casimir force. For this reason, we decided to indeed assume pairwise additivity for the critical Casimir interaction and neglect many-body effects of higher order. Although this approximation might negatively affect the quantitative accuracy of our theoretical predictions in comparison to possible experiments, we do not expect a considerable impact on the qualitative behavior.

All the following calculations are for colloids with $a = 3 \mu\text{m}$, $d = 3.1 \mu\text{m}$ [19] and $\chi_{\text{eff}} = 7.62 \times 10^{-11} \text{Am}^2\text{T}^{-1}$ [32] immersed in a water–2,6-Lutidine mixture with $T_c = 307 \text{K}$ and $\xi_0 = 0.2 \text{nm}$ [23]. Note that, because the colloids are confined to a flat monolayer by design, the thermodynamics of the system are essentially two-dimensional and will therefore have to be dealt with as such.

III. STATICS

A. Density Functional Theory

Let Ω_μ^{eq} be the grand potential of a two-dimensional grand-canonical ensemble with chemical potential μ and (one-particle) density distribution ρ_{eq} in equilibrium. Density functional theory (DFT) then asserts that there exists a unique functional Ω_μ of the density distribution ρ such that

$$\Omega_\mu^{\text{eq}} = \Omega_\mu[\rho_{\text{eq}}] < \Omega_\mu[\rho_{\text{ne}}] \quad (3)$$

for all $\rho_{\text{ne}} \neq \rho_{\text{eq}}$ [33]. For a two-dimensional system with area A and external potential V_{ext} , this functional can be written as

$$\Omega_\mu[\rho] = \mathcal{F}[\rho] + \int_A d^2\mathbf{r} [V_{\text{ext}}(\mathbf{r}) - \mu] \rho(\mathbf{r}), \quad (4)$$

where $\mathcal{F} = \mathcal{F}_{\text{id}} + \mathcal{F}_{\text{ex}}$ denotes the intrinsic Helmholtz free-energy functional of the system, split up into an ideal gas part \mathcal{F}_{id} and an excess part \mathcal{F}_{ex} . The ideal gas contribution is exactly known [34] to be

$$\mathcal{F}_{\text{id}}[\rho] = k_B T \int_A d^2\mathbf{r} \rho(\mathbf{r}) \{\ln[\Lambda^2 \rho(\mathbf{r})] - 1\}. \quad (5)$$

The choice of thermal wavelength is of no significance in our case; we used $\Lambda = \sqrt{\pi/4} d$ for convenience. The excess contribution depends on the interactions between the particles in the system and is for our model best expressed as $\mathcal{F}_{\text{ex}} = \mathcal{F}_{\text{ex}}^{\text{hd}} + \mathcal{F}_{\text{ex}}^{\text{ci}}$.

For the approximation of the electrostatic repulsion as a hard core with diameter $d > a$ we use the quite accurate hard disk functional

$$\mathcal{F}_{\text{ex}}^{\text{hd}}[\rho] = k_B T \int_A d^2\mathbf{r} \phi_{\text{hd}}[\mathbf{n}(\rho, \mathbf{r})] \quad (6)$$

from Ref. [35], where

$$\phi_{\text{hd}}(\mathbf{n}) = -\mathbf{n}_1 \ln(1 - \mathbf{n}_2) + \frac{19\mathbf{n}_3 \cdot \mathbf{n}_3 - 5\mathbf{n}_4 \cdot \mathbf{n}_4 - 14\mathbf{n}_5 \cdot \mathbf{n}_5}{48\pi (1 - \mathbf{n}_2)} \quad (7)$$

is a function of a set $\mathbf{n} = (\mathbf{n}_1, \dots, \mathbf{n}_5)$ of five weighted densities. Each weighted density \mathbf{n}_α is the convolution of a corresponding weight function ω_α with ρ ,

$$\mathbf{n}_\alpha(\rho, \mathbf{r}) = \int_A d^2\mathbf{r}' \rho(\mathbf{r}') \omega_\alpha(\mathbf{r} - \mathbf{r}'). \quad (8)$$

The weight functions are defined as

$$\begin{aligned} \omega_1(\mathbf{r}) &= \delta(d - 2|\mathbf{r}|)/(\pi d), \\ \omega_2(\mathbf{r}) &= \Theta(d - 2|\mathbf{r}|), \\ \omega_3(\mathbf{r}) &= \delta(d - 2|\mathbf{r}|), \\ \omega_4(\mathbf{r}) &= \delta(d - 2|\mathbf{r}|)\mathbf{r}/|\mathbf{r}|, \\ \omega_5(\mathbf{r}) &= \delta(d - 2|\mathbf{r}|)\mathbf{r}\mathbf{r}/|\mathbf{r}|^2, \end{aligned} \quad (9)$$

where δ is the Dirac delta function, Θ the Heaviside step function, and $\mathbf{r}\mathbf{r} \in \mathbb{R}^{2 \times 2}$ with $(\mathbf{r}\mathbf{r})_{ij} = x_i x_j$ for $\mathbf{r} = (x_1, x_2)$.

We treat the competing critical Casimir and magnetic dipole forces as a small perturbation to the hard core interaction and employ the random phase approximation (RPA)

$$\mathcal{F}_{\text{ex}}^{\text{ci}}[\rho] = \frac{1}{2} \int_A d^2\mathbf{r} \rho(\mathbf{r}) \int_A d^2\mathbf{r}' \rho(\mathbf{r}') V_{\text{ci}}(|\mathbf{r} - \mathbf{r}'|), \quad (10)$$

with

$$V_{\text{ci}}(r) = \begin{cases} V_{\text{cas}}(d) + V_{\text{mag}}(d) & \text{if } r \leq d, \\ V_{\text{cas}}(r) + V_{\text{mag}}(r) & \text{otherwise.} \end{cases} \quad (11)$$

The artificial extension of the potential into the hard core is an empirical correction to the systematic underestimation of correlations with RPA [36].

1. Grand-canonical minimization

Given a chemical potential μ , we now want a way to determine the equilibrium density distribution ρ_{eq} . Since we know that Ω_μ has a minimum at ρ_{eq} , it follows that the (functional) derivative of Ω_μ must vanish for ρ_{eq} . Hence, we have

$$\begin{aligned} 0 &= \beta \left. \frac{\delta \Omega_\mu[\rho]}{\delta \rho(\mathbf{r})} \right|_{\rho=\rho_{\text{eq}}} = \beta \left. \frac{\delta \mathcal{F}[\rho]}{\delta \rho(\mathbf{r})} \right|_{\rho=\rho_{\text{eq}}} + \beta V_{\text{ext}}(\mathbf{r}) - \beta \mu \\ &= \beta \left. \frac{\delta \mathcal{F}_{\text{id}}[\rho]}{\delta \rho(\mathbf{r})} \right|_{\rho=\rho_{\text{eq}}} + \beta \left. \frac{\delta \mathcal{F}_{\text{ex}}[\rho]}{\delta \rho(\mathbf{r})} \right|_{\rho=\rho_{\text{eq}}} + \beta V_{\text{ext}}(\mathbf{r}) - \beta \mu \\ &= \ln[\Lambda^2 \rho_{\text{eq}}(\mathbf{r})] - c^{(1)}(\rho_{\text{eq}}, \mathbf{r}) + \beta V_{\text{ext}}(\mathbf{r}) - \beta \mu \\ &= \ln \frac{\rho_{\text{eq}}(\mathbf{r})}{\rho_{\text{eq}}^{\text{b}}} - c^{(1)}(\rho_{\text{eq}}, \mathbf{r}) + \beta V_{\text{ext}}(\mathbf{r}) - \beta \mu_{\text{ex}}(\rho_{\text{eq}}^{\text{b}}), \end{aligned} \quad (12)$$

with $\beta = (k_B T)^{-1}$, the excess chemical potential

$$\mu_{\text{ex}}(\rho^{\text{b}}) = \mu - \mu_{\text{id}}(\rho^{\text{b}}) = \mu - k_B T \ln(\Lambda^2 \rho^{\text{b}}), \quad (13)$$

the bulk density

$$\rho^b = \frac{1}{A} \int d^2\mathbf{r} \rho(\mathbf{r}), \quad (14)$$

and the one-body direct correlation function

$$c^{(1)}(\rho, \mathbf{r}) = -\frac{\delta \mathcal{F}_{\text{ex}}[\rho]}{\delta \rho(\mathbf{r})}. \quad (15)$$

One finds that $c^{(1)}(\rho, \mathbf{r}) = c_{\text{hd}}^{(1)}(\rho, \mathbf{r}) + c_{\text{ci}}^{(1)}(\rho, \mathbf{r})$, where

$$c_{\text{hd}}^{(1)}(\rho, \mathbf{r}) = -\sum_{\alpha=1}^5 \int_A d^2\mathbf{r}' \frac{\partial \phi_{\text{hd}}(\mathbf{n})}{\partial \mathbf{n}_\alpha} \Big|_{\mathbf{n}=\mathbf{n}(\rho, \mathbf{r}')} \omega_\alpha(\mathbf{r}' - \mathbf{r}) \quad (16)$$

and

$$c_{\text{ci}}^{(1)}(\rho, \mathbf{r}) = -\int_A d^2\mathbf{r}' \rho(\mathbf{r}') \beta V_{\text{ci}}(|\mathbf{r} - \mathbf{r}'|). \quad (17)$$

We can now recast Eq. (12) into the self-consistency relation

$$\rho_{\text{eq}}(\mathbf{r}) = \rho_{\text{eq}}^b \exp[c^{(1)}(\rho_{\text{eq}}, \mathbf{r}) - \beta V_{\text{ext}}(\mathbf{r}) + \beta \mu_{\text{ex}}(\rho_{\text{eq}}^b)] \quad (18)$$

and use it in a Picard iteration to minimize Ω_μ . Starting with an initial density distribution ρ_0 , we successively generate a series $(\rho_i)_{i \in \mathbb{N}}$ via

$$\rho_{i+1}(\mathbf{r}) = \alpha_i \rho_i^b \exp[c^{(1)}(\rho_i, \mathbf{r}) - \beta V_{\text{ext}}(\mathbf{r}) + \beta \mu_{\text{ex}}(\rho_i^b)] + (1 - \alpha_i) \rho_i(\mathbf{r}), \quad (19)$$

where the mixing parameters $\alpha_i \in (0, 1)$ are chosen such that $\Omega_\mu[\rho_{i+1}] < \Omega_\mu[\rho_i]$ for all $i \in \mathbb{N}$, and stop once a convergence criterion is satisfied. Of course, there is no guarantee that one arrives at the thermodynamically stable global minimum of Ω_μ ; it is just as well possible to reach a metastable local minimum. The destination primarily depends on the starting point, and choosing a suitable ρ_0 may involve some educated guessing.

This minimization procedure can be considered grand-canonical in the sense that it yields the grand potential as a function of the chemical potential, which is very handy for determining phase coexistence. If Ω_μ has two different minima ρ_{eq}^A and ρ_{eq}^B with equal pressure $P_\mu[\rho_{\text{eq}}^A] = P_\mu[\rho_{\text{eq}}^B]$, where $P_\mu[\rho] = -\Omega_\mu[\rho]/A$, then the phases ‘‘A’’ and ‘‘B’’ can coexist.

2. Quasicanonical minimization

Because the chemical potential is a rather hard quantity to grasp, it can be more practical to replace μ with the equilibrium bulk density ρ_{eq}^b or, equivalently, the particle number

$$\mathcal{N}[\rho] = A\rho^b = \int_A d^2\mathbf{r} \rho(\mathbf{r}) = -\frac{\partial \Omega_\mu[\rho]}{\partial \mu}, \quad (20)$$

by minimizing the Helmholtz free-energy functional

$$\begin{aligned} \mathcal{A}[\rho] &= \Omega_\mu[\rho] - \mu \frac{\partial \Omega_\mu[\rho]}{\partial \mu} = \Omega_\mu[\rho] + \mu \mathcal{N}[\rho] \\ &= \mathcal{F}[\rho] + \int_A d^2\mathbf{r} V_{\text{ext}}(\mathbf{r}) \rho(\mathbf{r}), \end{aligned} \quad (21)$$

which is the Legendre transform of Ω_μ with respect to μ , under the constraint that $\mathcal{C}[\rho] = 0$ for

$$\mathcal{C}[\rho] = \int_A d^2\mathbf{r} \rho(\mathbf{r}) - \rho_{\text{eq}}^b A. \quad (22)$$

This is accomplished by minimization of the modified functional

$$\begin{aligned} \mathcal{A}'[\rho] &= \mathcal{A}[\rho] - \gamma \mathcal{C}[\rho] \\ &= \mathcal{F}[\rho] + \int_A d^2\mathbf{r} [V_{\text{ext}}(\mathbf{r}) - \gamma] \rho(\mathbf{r}) + \gamma \rho_{\text{eq}}^b A, \end{aligned} \quad (23)$$

which, in equilibrium, gives us

$$\begin{aligned} 0 &= \beta \frac{\delta \mathcal{A}'[\rho]}{\delta \rho(\mathbf{r})} \Big|_{\rho=\rho_{\text{eq}}} = \beta \frac{\delta \mathcal{F}[\rho]}{\delta \rho(\mathbf{r})} \Big|_{\rho=\rho_{\text{eq}}} + \beta [V_{\text{ext}}(\mathbf{r}) - \gamma] \\ &= \ln[\Lambda^2 \rho_{\text{eq}}(\mathbf{r})] - c^{(1)}(\rho_{\text{eq}}, \mathbf{r}) + \beta V_{\text{ext}}(\mathbf{r}) - \beta \gamma. \end{aligned} \quad (24)$$

This can be rearranged into

$$\rho_{\text{eq}}(\mathbf{r}) = \frac{\exp(\beta \gamma)}{\Lambda^2} \exp[c^{(1)}(\rho_{\text{eq}}, \mathbf{r}) - \beta V_{\text{ext}}(\mathbf{r})] \quad (25)$$

and combined with $\mathcal{C}[\rho_{\text{eq}}] = 0$ to obtain

$$\frac{\exp(\beta \gamma)}{\Lambda^2} \int_A d^2\mathbf{r} \exp[c^{(1)}(\rho_{\text{eq}}, \mathbf{r}) - \beta V_{\text{ext}}(\mathbf{r})] = \rho_{\text{eq}}^b A, \quad (26)$$

allowing us to eliminate the Lagrange multiplier γ in Eq. (25) and arrive at the quasicanonical self-consistency equation

$$\rho(\mathbf{r}) = \rho_{\text{eq}}^b \frac{\exp[c^{(1)}(\rho_{\text{eq}}, \mathbf{r}) - \beta V_{\text{ext}}(\mathbf{r})]}{\frac{1}{A} \int_A d^2\mathbf{r}' \exp[c^{(1)}(\rho_{\text{eq}}, \mathbf{r}') - \beta V_{\text{ext}}(\mathbf{r}')]} \quad (27)$$

In analogy to the grand-canonical case, we construct a series $(\rho_i)_{i \in \mathbb{N}}$ with $\rho_i^b = \rho_{\text{eq}}^b$ and $\mathcal{A}[\rho_{i+1}] < \mathcal{A}[\rho_i]$ using the recurrence relation

$$\begin{aligned} \rho_{i+1}(\mathbf{r}) &= \alpha_i \rho_{\text{eq}}^b \frac{\exp[c^{(1)}(\rho_i, \mathbf{r}) - \beta V_{\text{ext}}(\mathbf{r})]}{\frac{1}{A} \int_A d^2\mathbf{r}' \exp[c^{(1)}(\rho_i, \mathbf{r}') - \beta V_{\text{ext}}(\mathbf{r}')]} \\ &\quad + (1 - \alpha_i) \rho_{\text{eq}}^b \frac{\rho_i(\mathbf{r})}{\frac{1}{A} \int_A d^2\mathbf{r}' \rho_i(\mathbf{r}')} \end{aligned} \quad (28)$$

and suitable mixing parameters $\alpha_i \in (0, 1)$.

B. Implementation

The calculation of many quantities such as $\mathcal{F}_{\text{ex}}^{\text{ci}}$, \mathbf{n}_α and $c_{\text{ci}}^{(1)}$ involves the convolution of the density distribution ρ with some other function f ,

$$g(\mathbf{r}) = \int_{A=L_x \times L_y} d^2\mathbf{r}' \rho(\mathbf{r}') f(\mathbf{r} - \mathbf{r}'). \quad (29)$$

These are rather expensive to compute in real space, but can be reduced to a simple and fast multiplication in Fourier space with the convolution theorem: The Fourier series coefficients of g are

$$\hat{g}_{mn} = \hat{\rho}_{mn} \hat{f}(\mathbf{k}_{mn}) \quad (30)$$

for $m, n \in \mathbb{Z}$ and $\mathbf{k}_{mn} = (m/L_x, n/L_y)$, where

$$\hat{\rho}_{mn} = \frac{1}{A} \int_A d^2\mathbf{r} \rho(\mathbf{r}) \exp(-i2\pi \mathbf{k}_{mn} \cdot \mathbf{r}) \quad (31)$$

are the Fourier series coefficients of ρ and

$$\hat{f}(\mathbf{k}) = \int_{\mathbb{R}^2} d^2\mathbf{r} f(\mathbf{r}) \exp(-i2\pi\mathbf{k} \cdot \mathbf{r}) \quad (32)$$

is the Fourier transform of f . Attention must be paid to the fact that this move to Fourier space treats the integral in Eq. (29) as if it extended over all of \mathbb{R}^2 , and ρ as if it were an (L_x, L_y) -periodic function with $\rho(\mathbf{r} + \mathbf{R}) = \rho(\mathbf{r})$ for $\mathbf{r} \in A$ and $\mathbf{R} \in \{(nL_x, mL_y) \mid n, m \in \mathbb{Z}\}$. This introduces infinitely many artificial mirror images of the original system which could potentially interfere with each other. The system must therefore be isolated, which can be achieved by truncating the competing interaction so that $V_{ci}(r) = 0$ for $r > r_{\max}^{ci} = (L_x^2 + L_y^2)^{1/2}$ (the maximum possible distance between two colloids), and enclosing the system in a hard wall of thickness $W = \max\{d, r_{\max}^{ci}\}/2$. To implement the wall, we increase the system size in both dimensions by $2W$ to $L'_x = L_x + 2W$ and $L'_y = L_y + 2W$, and impose the external potential

$$V_{\text{ext}}(\mathbf{r}) = \begin{cases} 0, & \text{if } \mathbf{r} \in [W, W + L_x] \times [W, W + L_y], \\ \infty, & \text{otherwise.} \end{cases} \quad (33)$$

We perform the grand-canonical and quasicanonical minimization on a workstation by discretizing density distributions on a regular grid with $N_x \times N_y$ lattice points and a resolution of $\min\{N_x/L'_x, N_y/L'_y\} \geq 20/d$. We combine the efficient fast Fourier transform algorithm with the parallel computing facilities of modern graphics processing units [37] to significantly accelerate the calculations.

C. Results

The search for stable microphases in a finite system required a certain amount of trial and error since we did not know what kind of structures to expect and look for. Naturally, we used our findings for the infinite system as a starting point, and at first considered something akin to a hexagonal cluster phase with one cluster in each of the four corners of the system and a fifth in the center to be feasible. The result of a quasicanonical minimization initialized with a hexagonal cluster pattern for the bulk packing fraction $\eta^b = (\pi/4)d^2\rho^b = 0.15$, magnetic field $B = 7.5 \mu\text{T}$, temperature $T = T_c - 0.16$ and $L_y = 39.5d = \sqrt{3}L_x$ can be seen in Fig. 2(a). While the effects of the competing interactions are clearly evident in that the clusters do not diffuse away but actually prevail, the center cluster surprisingly moves to the right edge and the clusters in the left corners acquire a slightly different shape compared to their counterparts on the other side. This breaks the horizontal mirror symmetry and also the twofold rotational symmetry, suggesting a metastable state; and indeed, when the minimization is started with a flat density profile instead, one reaches the configuration shown in Fig. 2(b), which features two opposing stripes or elongated clusters (the distinction is not really clear in this case) close and parallel to either one or the other short side, offers the expected symmetry, and has a lower Helmholtz free energy. For lower η^b we have found a phase with only four clusters [one in each corner; see Fig. 2(c)], whereas for higher η^b a closed ring formed along the walls [Fig. 2(d)].

Since we were unable to stabilize a hexagonal arrangement of clusters, it seemed arbitrary to stick to $L_y/L_x = \sqrt{3}$,

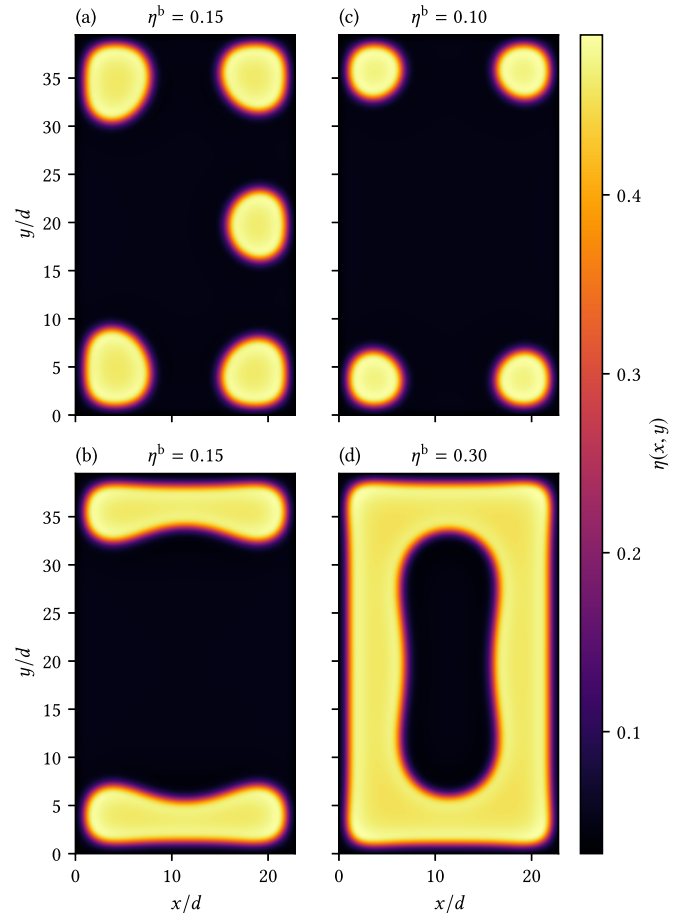


FIG. 2. Density profiles for a cell with $L_y = 39.5d = \sqrt{3}L_x$, magnetic field $B = 7.5 \mu\text{T}$ and temperature $T = T_c - 0.16$ K. For the bulk packing fraction $\eta^b = 0.15$, the quasicanonical minimization reaches an asymmetric, metastable state when initialized with a hexagonal pattern (a); starting with a flat, uniform density distribution leads to a symmetric stripe phase with a lower Helmholtz free energy (b). For $\eta^b = 0.10$, a cluster emerges in each of the four corners, whereas a ring forms for $\eta^b = 0.30$ (d).

which was of course initially chosen precisely because it is the aspect ratio of a rectangular unit cell for a hexagonal lattice. We therefore decided to continue with a square cell, $L_x = L_y = L$. To assess the impact of the system size, we looked at both $L = 20d$ and $L = 30d$. For $L_x = L_y$, we have likewise found a cluster phase for lower η^b [Figs. 3(b) and 3(f) for $L = 30d$ and Fig. 4(a) for $L = 20d$] and a ring phase for higher η^b [Figs. 3(c) and 3(g) for $L = 30d$ and Fig. 4(b) for $L = 20d$]. However, we did not discover a stripe phase as we did for $L_y = \sqrt{3}L_x$; this makes sense, though, because a square geometry has a 4-fold rotational symmetry that would be broken by a stripe pattern. For very low and very high η^b , the system loses any distinct patterns and acts as an almost uniform vapor [Figs. 3(a) and 3(e)] or liquid [Figs. 3(d) and 3(h)], respectively.

For $L = 30d$ and higher magnetic fields, the ring phase can assume a curious variety of shapes upon increasing η^b : While for $B = 8.7 \mu\text{T}$ and $\eta^b = 0.19$, we have a rather thin ring that encloses a roughly square region [Fig. 3(g)], this region morphs into a four-leaf clover for $\eta^b = 0.28$, a horseshoe for

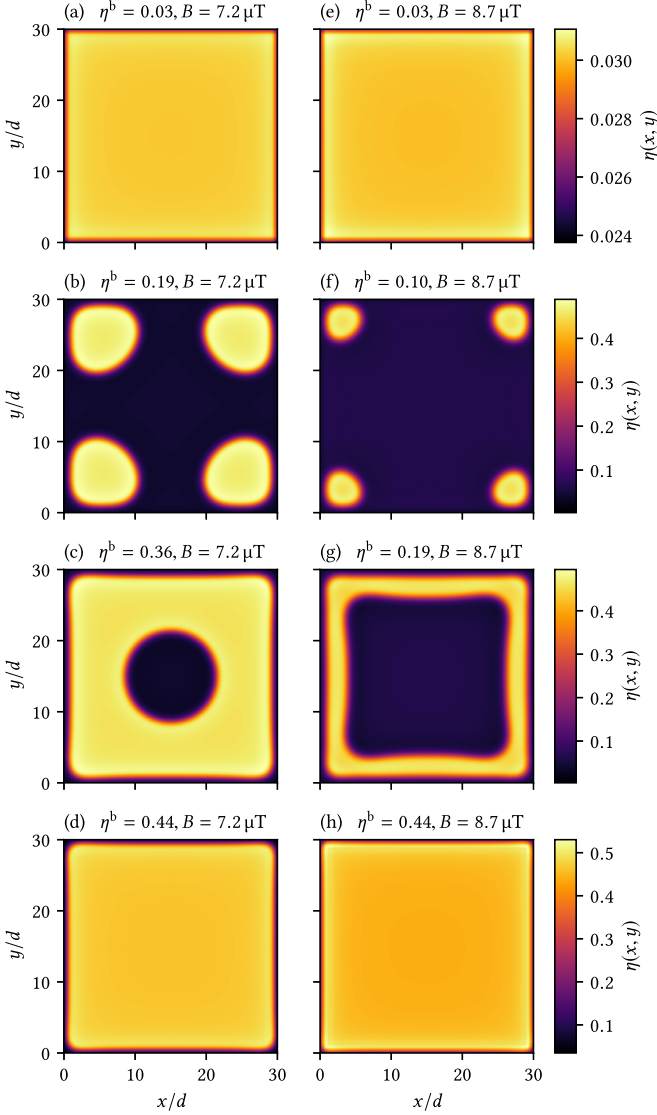


FIG. 3. Equilibrium density profiles for a square cell with side length $L = 30d$, temperature $T = T_c - 0.16$ K and various values of the magnetic field strength B and the bulk packing fraction η^b . With increasing η^b , we can observe a vapor phase [(a) and (e)], a cluster phase [(b) and (f)], a ring phase [(c) and (g)] and a liquid phase [(d) and (h)].

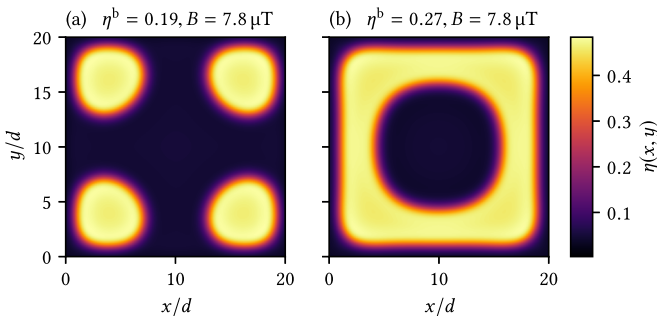


FIG. 4. Equilibrium density profiles for a square cell with side length $L = 20d$, temperature $T = T_c - 0.16$ K and magnetic field strength $B = 7.8 \mu\text{T}$. We find a cluster phase for the bulk packing fraction $\eta^b = 0.19$ (a) and a ring phase for $\eta^b = 0.27$ (b).

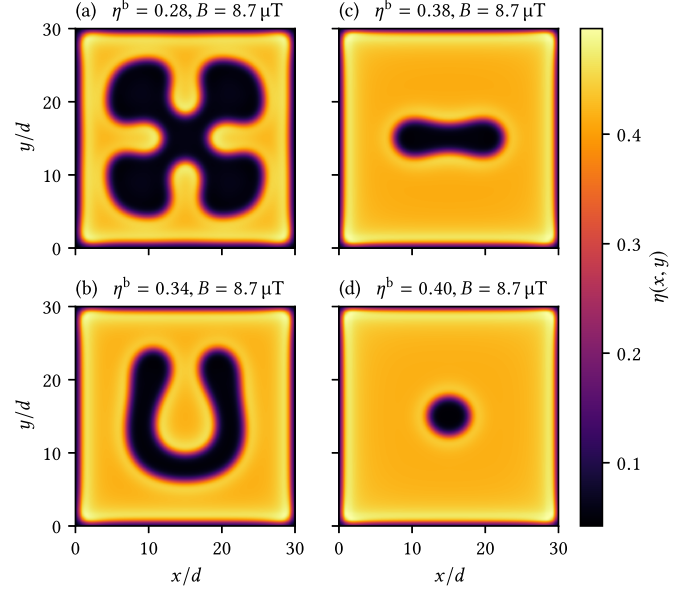


FIG. 5. Different manifestations of the ring phase for a square cell with side length $L = 30d$, temperature $T = T_c - 0.16$ K, and magnetic field strength $B = 8.7 \mu\text{T}$. The region enclosed by the ring looks like a four-leaf clover for $\eta^b = 0.28$ (a), a horseshoe for $\eta^b = 0.34$ (b), a slit for $\eta^b = 0.38$ (c), and a small disk for $\eta^b = 0.40$ (d).

$\eta^b = 0.34$, and a slit for $\eta^b = 0.38$ before ending up as a small disk for $\eta^b = 0.40$ [Figs. 5(a)–5(d), respectively]. The fact that the slit violates the fourfold rotational symmetry and the horseshoe also the vertical mirror symmetry may indicate that the ring phase is only metastable for intermediate bulk packing fractions and that more stable phases exist of which we are not aware; but this is hard to test as it necessitates correctly guessing *a priori* how these phases might look like.

The observation that clusters and rings tend to form in the corners or along the walls of the cell, respectively, can be explained by the long-ranged repulsion between the colloids: Since there are no particles outside the cell to compensate the repulsion within, the structures are pushed apart toward the system border [38].

The effects of confinement in systems with microphase separation have already been the target of several studies. Serna *et al.* investigated a three-dimensional colloidal system with competing interactions and focused on the hexagonal cylindrical phase [39], which is similar to the two-dimensional hexagonal cluster phase extended in the perpendicular direction. They found that this phase can also be stable when confined to channels with hard walls and a triangular or hexagonal cross-section, i.e., a shape compatible with the equilibrium pattern in the bulk; it would not be surprising if we saw the same behavior in our system, but we have so far only looked at rectangular cell geometries. For square cross-sections, the cylinders form in some cases a square lattice comparable to the cluster phase we observed in a square cell; however, whereas we never encountered a stable phase with more than four clusters, this restriction does not seem to hold for cylinders. Interestingly, for larger chemical potentials (and thus particle densities), Serna *et al.* also found analogs of

the ring phase in the form of (possibly multiple concentric) tubes parallel to the channels. Pękalski *et al.* likewise observed concentric rings in their study of a two-dimensional triangular lattice model with competing interactions in hexagonal confinement [40]. In a two-dimensional system with a short-ranged Yukawa attraction, long-ranged Coulomb repulsion and a circular logarithmic trap, Xu *et al.* found cluster and ring structures along with other more exotic ones [41]; similar patterns emerged in a two-dimensional system studied by Liu *et al.*, featuring a short-ranged exponential attraction, long-ranged Yukawa repulsion and circular quadratic trap [42].

Without making any claims as to their completeness, we have calculated phase diagrams for $T = T_c - 0.16$ K that incorporate the vapor, cluster, ring and liquid phases by determining their points of coexistence for a range of magnetic field strengths B . For two adjacent phases “A” and “B”, we vary μ until we find the coexistence chemical potential μ_c for which the corresponding equilibrium density distributions ρ_{eq}^A and ρ_{eq}^B give rise to the same pressure, $P_{\mu_c}[\rho_{\text{eq}}^A] = P_{\mu_c}[\rho_{\text{eq}}^B]$. The bulk packing fractions of the states of coexistence are then plotted versus the associated magnetic field. The resulting phase diagram for $L = 30d$ is displayed in Fig. 6(a), that for $L = 20d$ in Fig. 6(b). Both look very similar and show that the cluster phase is remarkably narrow with regard to η^b in relation to the ring phase and that it borders on rather wide regions of coexistence, especially for lower B . This stands in marked contrast the phase diagram for the infinite system in Ref. [18], where the width of the cluster, lamellar and bubble phases are almost equal and the gap separating them is comparatively thin. The difference in width between the cluster and the ring phase may indicate that both the lamellar and bubble patterns morph into a ring structure when confined to a square geometry.

The phase diagram for $L = 30d$ offers an interesting feature that the one for $L = 20d$ does not have: The cluster and ring phases overlap to some extent in that for a small range of bulk packing fractions, $0.17 \lesssim \eta^b \lesssim 0.20$, the system can be in either of the two phases, depending on the magnetic field; this means that it should be possible to induce a transition from one phase to the other by altering B while keeping η^b constant, which is something to keep in mind for our study of the dynamics that is about to follow.

IV. DYNAMICS

A. Dynamic density functional theory

The trajectories $[\mathbf{r}_i(t)]_{i \in \{1, \dots, N\}}$ of a system of N colloids submerged in a solvent can be described by a coupled set of Langevin equations,

$$m \frac{d^2 \mathbf{r}_i(t)}{dt^2} = -\nabla V_{\text{ext}}(\mathbf{r}_i) - \nabla \sum_{j=1}^N V_{\text{int}}(|\mathbf{r} - \mathbf{r}_j|) - \gamma \frac{d\mathbf{r}_i(t)}{dt} + \boldsymbol{\varphi}_i(t), \quad (34)$$

where the terms on the right-hand side correspond to the external force acting on the i th colloid, the interparticles forces due to the pair interaction potential V_{int} , the Stokes drag with friction coefficient γ , and a stochastic force $\boldsymbol{\varphi}_i$ to account

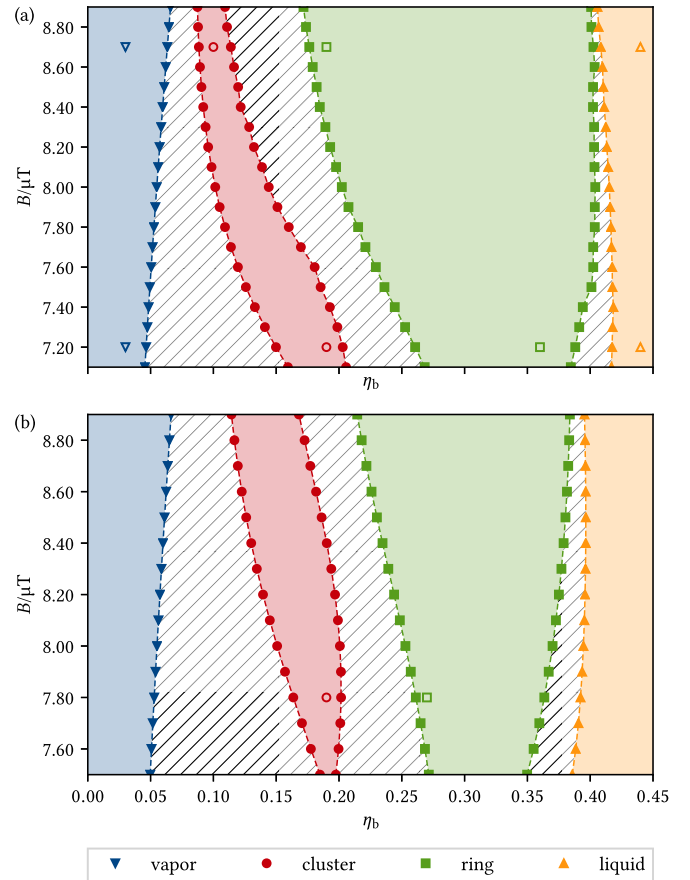


FIG. 6. Phase diagrams for a square cell with $L = 30d$ (a) and $L = 20d$ (b) at temperature $T = T_c - 0.16$ K. Filled symbols show the magnetic field strength B and bulk packing fraction η^b of the coexistence states of adjacent phases; the regions of coexistence in between are hatched. Unfilled symbols mark the state points for the density profiles shown in Figs. 3 and 4. For $L = 30d$, but not for $L = 20d$, the cluster and ring phases overlap to some extent in that for certain η^b ($0.17 \lesssim \eta^b \lesssim 0.20$), the system can be in either of the two phases, depending on B .

for the thermal agitation of the colloid as a result of random collisions with the molecules of the solvent. For colloids, the drag is so large that, compared to the time scales we are interested in, any inertial motion is damped down practically immediately. We can therefore consider the left-hand side to be negligible and find that

$$\gamma \frac{d\mathbf{r}_i(t)}{dt} = -\nabla \left[V_{\text{ext}}(\mathbf{r}_i) + \sum_{j \neq i} V_{\text{int}}(|\mathbf{r} - \mathbf{r}_j|) \right] + \boldsymbol{\varphi}_i(t). \quad (35)$$

Solving this stochastic differential equation and defining the instantaneous density distribution at time t as

$$\rho_t(\mathbf{r}) = \left\langle \sum_{i=1}^N \delta[\mathbf{r} - \mathbf{r}_i(t)] \right\rangle, \quad (36)$$

where $\langle \cdot \rangle$ denotes the average over all possible realization of the stochastic force, one can derive [43–45] that

$$\gamma \frac{\partial \rho_t(\mathbf{r})}{\partial t} = \nabla \left[k_B T \nabla \rho_t(\mathbf{r}) + \rho_t(\mathbf{r}) \nabla V_{\text{ext}}(\mathbf{r}) + \int d^2 \mathbf{r}' \rho_t^{(2)}(\mathbf{r}, \mathbf{r}') \nabla V_{\text{int}}(\mathbf{r} - \mathbf{r}') \right]. \quad (37)$$

Unfortunately, the instantaneous two-particle density distribution

$$\rho_t^{(2)}(\mathbf{r}, \mathbf{r}') = \left\langle \sum_{i,j=1}^N \delta[\mathbf{r} - \mathbf{r}_i(t)] \delta[\mathbf{r}' - \mathbf{r}_j(t)] \right\rangle \quad (38)$$

is not known in general. An approximation that has proved quite successful is to use the exact equilibrium relation

$$\int d^2 \mathbf{r}' \rho_{\text{eq}}^{(2)}(\mathbf{r}, \mathbf{r}') \nabla V_{\text{int}}(\mathbf{r} - \mathbf{r}') = -k_B T \rho_{\text{eq}}(\mathbf{r}) \nabla c^{(1)}(\rho_{\text{eq}}, \mathbf{r}) \quad (39)$$

also in nonequilibrium by replacing ρ_{eq} with ρ_t . Equation (37) can then be cast into the continuity equation

$$\frac{\partial \rho_t(\mathbf{r})}{\partial t} = -\nabla \cdot \mathbf{j}_t(\mathbf{r}), \quad (40)$$

with the instantaneous particle current

$$\begin{aligned} \mathbf{j}_t(\mathbf{r}) &= -D \{ \nabla \rho_t(\mathbf{r}) + \rho_t(\mathbf{r}) \nabla [\beta V_{\text{ext}}(\mathbf{r}) - c^{(1)}(\rho_t, \mathbf{r})] \} \\ &= -D \rho_t(\mathbf{r}) \beta \nabla \frac{\delta \mathcal{A}[\rho_t]}{\delta \rho_t(\mathbf{r})}, \end{aligned} \quad (41)$$

where $D = k_B T / \gamma$ is the diffusion coefficient and \mathcal{A} is the Helmholtz free-energy functional. This is the central result of density functional theory (DDFT) that, given an initial density profile ρ_0 at $t = 0$, allows us to compute the time evolution of ρ_t by (numerically) integrating Eq. (40).

It is worth noting that the dynamics correctly preserve the number of particles in a closed system since

$$\begin{aligned} \frac{d\mathcal{N}[\rho_t]}{dt} &= \int_A d^2 \mathbf{r} \frac{d\rho_t(\mathbf{r})}{dt} = - \int_A d^2 \mathbf{r} \nabla \cdot \mathbf{j}_t(\mathbf{r}) \\ &= - \int_{\partial A} d\mathbf{A}(\mathbf{r}) \cdot \mathbf{j}_t(\mathbf{r}) = 0, \end{aligned} \quad (42)$$

because $\rho_t(\mathbf{r}) = 0$ and therefore $\mathbf{j}_t(\mathbf{r}) = 0$ for $\mathbf{r} \in \partial A$. Furthermore, it is easily shown that

$$\begin{aligned} \frac{d\mathcal{A}[\rho_t]}{dt} &= \int_A d^2 \mathbf{r} \frac{\delta \mathcal{A}[\rho_t]}{\delta \rho_t(\mathbf{r})} \frac{\partial \rho_t(\mathbf{r})}{\partial t} \\ &= -\beta D \int_A d^2 \mathbf{r} \rho_t(\mathbf{r}) \left[\nabla \frac{\delta \mathcal{A}[\rho_t]}{\delta \rho_t(\mathbf{r})} \right]^2 \leq 0, \end{aligned} \quad (43)$$

which means that the Helmholtz free energy will only ever decrease over time. Last, if $\rho_0 = \rho_{\text{eq}}$, then $\rho_t = \rho_{\text{eq}}$ and $\mathcal{A}[\rho_t] = \mathcal{A}[\rho_{\text{eq}}]$ for all t , because

$$\frac{\delta \mathcal{A}[\rho_{\text{eq}}]}{\delta \rho_{\text{eq}}(\mathbf{r})} = 0. \quad (44)$$

B. Implementation

As in the static case, many calculations are more easily performed in Fourier space. This of course again includes

any convolutions, but also the spatial derivatives that enter in Eqs. (40) and (41): The Fourier transform of $\mathbf{g}(\mathbf{r}) = \nabla f(\mathbf{r})$ for some function f is simply $\hat{\mathbf{g}}(\mathbf{k}) = i\mathbf{k}\hat{f}(\mathbf{k})$.

Furthermore, Eq. (40) can be more accurately integrated in Fourier space using a method known as exponential time differencing [46,47]. Expressing this equation in real space as

$$\frac{1}{D} \frac{\partial \rho_t(\mathbf{r})}{\partial t} = \nabla^2 \rho_t(\mathbf{r}) + \sigma_t(\mathbf{r}), \quad (45)$$

with $\sigma_t(\mathbf{r}) = \nabla \cdot [\rho_t(\mathbf{r}) \nabla \{\beta V_{\text{ext}}(\mathbf{r}) - c^{(1)}(\rho_t, \mathbf{r})\}]$, its Fourier transform is given by

$$\frac{1}{D} \frac{\partial \hat{\rho}_t(\mathbf{k})}{\partial t} = -\mathbf{k}^2 \hat{\rho}_t(\mathbf{k}) + \hat{\sigma}_t(\mathbf{k}). \quad (46)$$

Formally, this differential equation has the exact solution

$$\begin{aligned} \hat{\rho}_{t+\Delta t}(\mathbf{k}) &= \hat{\rho}_t(\mathbf{k}) \exp(-D\mathbf{k}^2 \Delta t) \\ &+ \int_0^{\Delta t} d\tau D \hat{\sigma}_{t+\tau}(\mathbf{k}) \exp[-D\mathbf{k}^2(\Delta t - \tau)], \end{aligned} \quad (47)$$

which is not that useful, unfortunately, since the right-hand side implicitly depends on $\hat{\rho}_{t+\tau}$ for $\tau \in [0, \Delta t]$ through $\hat{\sigma}$. However, if Δt is sufficiently small so that $\hat{\sigma}_{t+\tau} \simeq \hat{\sigma}_t$ for $\tau \in [0, \Delta t]$, then we can approximate the integral analytically and arrive at

$$\begin{aligned} \hat{\rho}_{t+\Delta t}(\mathbf{k}) &\simeq \hat{\rho}_t(\mathbf{k}) \exp(-D\mathbf{k}^2 \Delta t) \\ &+ \frac{\hat{\sigma}_t(\mathbf{k})}{\mathbf{k}^2} [1 - \exp(-D\mathbf{k}^2 \Delta t)]. \end{aligned} \quad (48)$$

We use this relation to successively evolve ρ_t in time with steps of $\Delta t / \tau_B = 5 \times 10^{-4}$, where $\tau_B = d^2 / D$ is the so-called Brownian time; this appeared to give a good accuracy at moderate computational costs. We check that every step indeed lowers the Helmholtz free energy as per Eq. (43).

DDFT is incompatible with the hard walls as implemented for the statics because the external potential and the density distribution have a discontinuity at the wall, and the spatial derivatives in Eq. (41) become therefore ill-defined. To avoid this problem, we slightly soften the wall up by introducing a thin transition area of thickness w between the proper system and the wall where the external potential smoothly increases from $V_{\text{ext}}^{\text{trans}}(0) = 0$ to $V_{\text{ext}}^{\text{trans}}(w) = V_{\text{ext}}^{\text{wall}}$ according to

$$V_{\text{ext}}^{\text{trans}}(z) = \left(-20 \frac{z^7}{w^7} + 70 \frac{z^6}{w^6} - 84 \frac{z^5}{w^5} + 35 \frac{z^4}{w^4} \right) V_{\text{ext}}^{\text{wall}}. \quad (49)$$

In this case, the competing interaction potential should be truncated to $r_{\text{max}}^{\text{ci}} = [(L_x + 2w)^2 + (L_y + 2w)^2]^{1/2}$ and the effective system size increased to $L'_x = L_x + 2(W + w)$ and $L'_y = L_y + 2(W + w)$ with $W = \max\{d, r_{\text{max}}^{\text{ci}}\}/2$. Since a continuous external potential requires $V_{\text{ext}}^{\text{wall}} < \infty$, we use $V_{\text{ext}}^{\text{wall}} = 50 k_B T$, which is sufficiently high to practically prevent the particles from overcoming the walls. In combination with $w = d$, this soft wall is barely distinguishable from a hard wall while still allowing for well-behaved dynamics.

C. Results

Our study of the dynamics focused on the reaction of the system to changes of B and T while keeping L and η^b fixed.

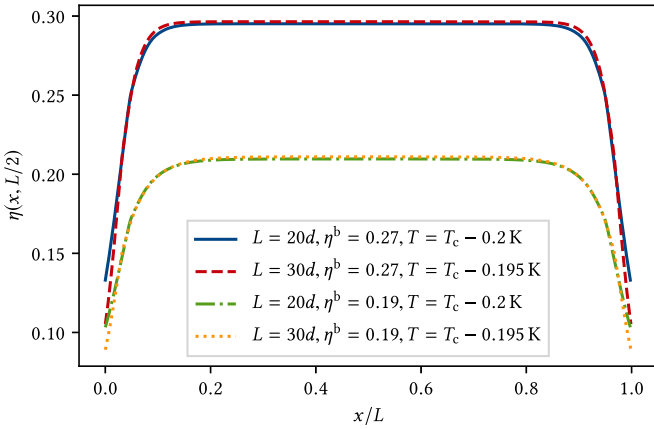


FIG. 7. Density profile for $y = L/2$ of the fluid configurations with $B = 0$ used as the initial states for the dynamics. For equal bulk packing fractions, the profiles for $L = 20d$ and $T = T_c - 0.2$ K are very similar to those for $L = 30d$ and $T = T_c - 0.195$ K. At equal temperatures, the differences would be more significant.

More precisely, we wanted to answer the following question: Starting out with some initial equilibrium state at $(B_i, T_i) = (B_i, T_i)$ for $t < 0$, how do we need to vary the magnetic field and temperature over time to eventually reach the stable configuration at a given final state $(B_f, T_f) = (B_f, T_f)$ for $t \rightarrow \infty$? We were particularly interested in paths that lead from stable liquid states with only weak attraction and no repulsion (and hence no competing interactions) into the microphase regime, ideally arriving at the cluster and ring phases discussed in Sec. III. For $L = 30d$, $\eta^b = 0.19$, and $T_f = T_c - 0.16$ K, we targeted the cluster state at $B_f = 7.2 \mu\text{T}$ [Fig. 3(b)] and the ring state at $B_f = 8.7 \mu\text{T}$ [Fig. 3(g)], whereas for $L = 20d$, $T_f = T_c - 0.16$ K and $B_f = 7.8 \mu\text{T}$, we aimed for the cluster state at $\eta^b = 0.19$ [Fig. 4(a)] and the ring state at $\eta^b = 0.27$ [Fig. 4(b)]. We chose the fluid configuration at $B_i = 0$ and $T_i = T_c - 0.195$ K as starting point for $L = 30d$, and $T_i = T_c - 0.2$ K for $L = 20d$. We opted for these slightly different temperatures because the initial density distributions for $L = 20d$ and $L = 30d$ are then qualitatively very similar for equal bulk packing fractions, as demonstrated by Fig. 7.

The most direct way to transition from (B_i, T_i) to (B_f, T_f) is to perform an instantaneous, discontinuous jump at $t = 0$,

$$(B_t, T_t) = \begin{cases} (B_i, T_i) & \text{for } t < 0, \\ (B_f, T_f) & \text{otherwise.} \end{cases} \quad (50)$$

Figure 8 shows what happens when this method is used in an attempt to go from the fluid to the cluster state for $L = 30d$. After a short time [$t/\tau_B = 10$, Fig. 8(b)] the increased attraction, as a consequence of abruptly raising the temperature closer toward T_c , causes the particles to aggregate into numerous small clusters and thin stripes. The structures in the center of the system then coalesce into two rings, whereas the outer stripes contract and separate from the clusters in the corners [$t/\tau_B = 30$, Fig. 8(c)]. Eventually, the two central rings merge into one large cluster and the outer stripes shrink into a roughly elliptical shape, resulting in a total of nine cluster of different sizes kept apart by the magnetic repulsion [$t/\tau_B = 900$, Fig. 8(d)]. This configuration is only metastable since it has a higher Helmholtz free energy than the one with

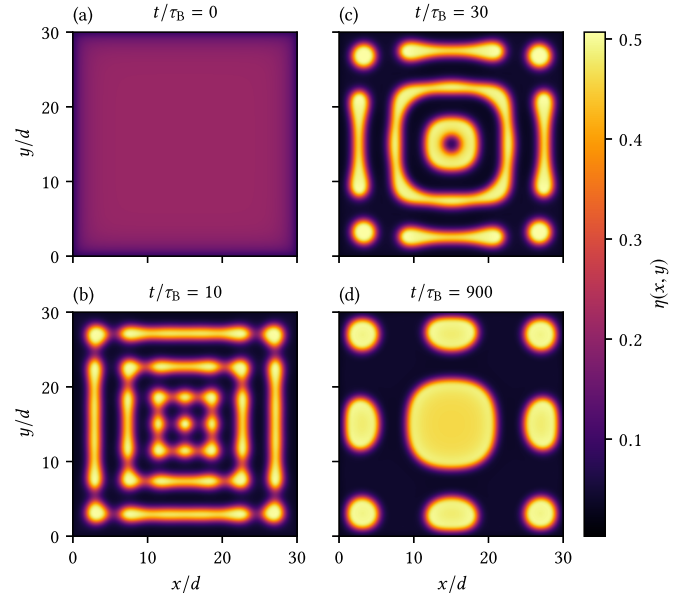


FIG. 8. Dynamic evolution of the density profile of a system with $L = 30d$ and $\eta^b = 0.19$ after equilibrating into a fluid state at $B = 0$ and $T = T_c - 0.195$ K (a), and then abruptly setting $B = 7.2 \mu\text{T}$ and $T = T_c - 0.16$ K at $t = 0$. See the Supplemental Material [48] for an animation.

only four clusters [Fig. 3(b)]. We have seen the same general behavior also when targeting the ring phase or when $L = 20d$.

The observed tendency that, for a liquid initial density profile, the sudden imposition of competing interactions first leads to the formation of many small agglomerations due to the strong short-range attraction, which then combine until they are large enough for the weak long-range repulsion to take over, presents in our view the biggest hurdle for the emergence of stable configurations in a dynamic evolution the system. This would especially concern experiments, where any slight asymmetry would only become more pronounced over time, causing a haphazard growth of highly irregular structures.

We next checked whether it would be an improvement to continuously transition from the initial to the final parameters over some nonzero but finite time τ_t . The simplest choice is to connect (B_f, T_f) and (B_i, T_i) through a linear path, i.e.,

$$(B_t, T_t) = \begin{cases} (B_i, T_i) & \text{for } t < 0, \\ (B_i, T_i) + (\Delta B, \Delta T) \frac{t}{\tau_t} & \text{for } 0 \leq t < \tau_t, \\ (B_f, T_f) & \text{otherwise,} \end{cases} \quad (51)$$

with $\Delta B = B_f - B_i$ and $\Delta T = T_f - T_i$. This indeed turned out to be a successful strategy for reaching the ring phase, as demonstrated by Fig. 9 for $L = 30d$. Due to the increasing attraction, the colloids are first drawn toward the center of the cell and begin to form a smaller squarish ring that is thicker near the corners. Over time, the thickness equalizes and the ring starts to grow in diameter as the repulsion between opposite points of the ring becomes stronger. After about $2000 \tau_B$, the system has essentially reached the stable equilibrium [cf. Figs. 9(h) and 3(g)]. Figure 10 shows the magnetic field and the temperature as a function of time. We chose a transition time of $\tau_t = 1000 \tau_B$, which seemed to be near the lower

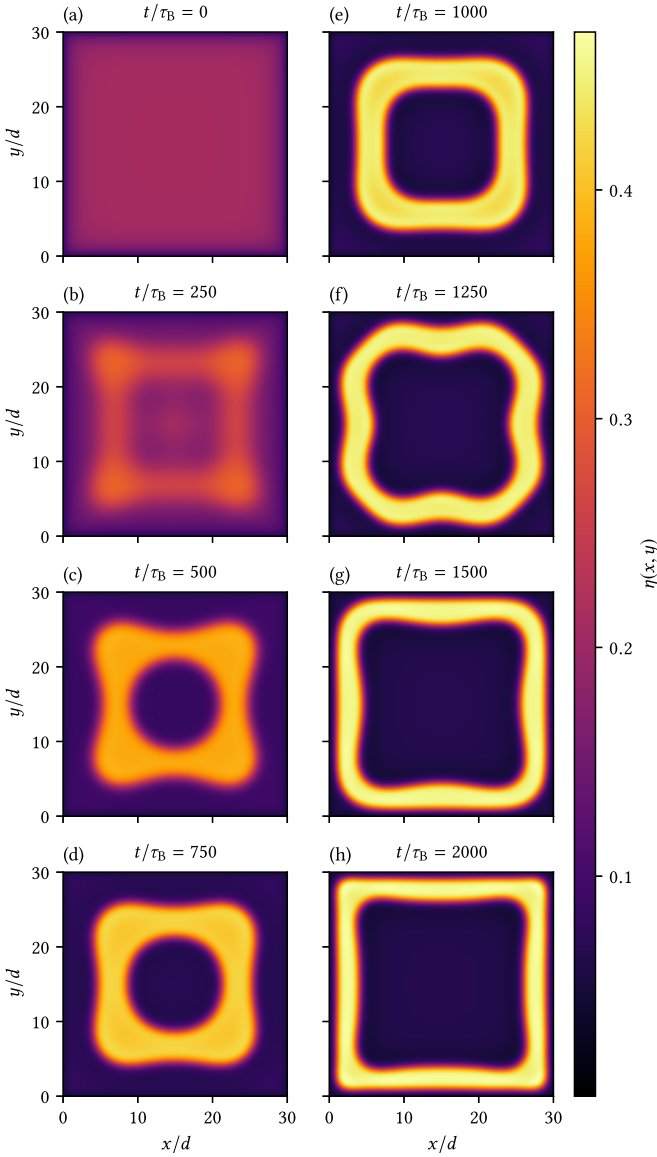


FIG. 9. Dynamic evolution of the density profile of a system with $L = 30d$ and $\eta^b = 0.19$ after equilibrating into a fluid state at $B = 0$ and $T = T_c - 0.195$ K (a), and then going quasilinearly to $B = 8.7 \mu\text{T}$ and $T = T_c - 0.16$ K during the period $[0, 1000 \tau_B]$ as shown in Fig. 10. After about $2000 \tau_B$, the system has practically reached the stable ring configuration [cf. panel (h) and Fig. 3(g)]. See the Supplemental Material [48] for an animation.

end of the range of values that produce a ring. Since regular recalculation of the competing interactions can become quite expensive, we approximated Eq. (51) with a staircase function of step length $\tau_s = 5 \tau_B$,

$$(B_t, T_t) = \begin{cases} (B_i, T_i) & \text{for } t < 0, \\ (B_i, T_i) + (\Delta B, \Delta T) \frac{[t/\tau_s]}{\tau_i/\tau_s} & \text{for } 0 \leq t < \tau_i, \\ (B_f, T_f) & \text{otherwise,} \end{cases} \quad (52)$$

which significantly reduces the frequency of the required updates.

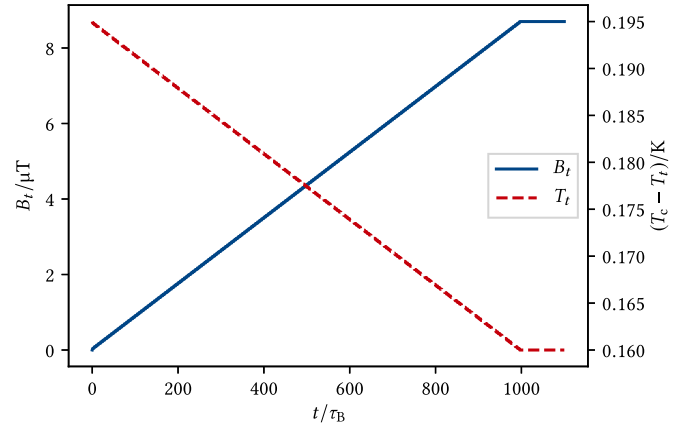


FIG. 10. Magnetic field B_t and temperature T_t as a function of time t during the dynamic evolution from the fluid to the ring configuration for $L = 30d$ and $\eta^b = 0.19$ shown in Fig. 9.

We observed a high sensitivity to the choice of the initial state. For example, if we start with a slightly lower temperature, $T_i = T_c - 0.20$ K, then the initial density profile is too uniform [Fig. 11(a)] and a cluster develops in the middle of the ring [Fig. 11(b)]; if, however, we set out with a marginally higher temperature, $T_i = T_c - 0.19$ K, then the colloids are too concentrated near the center [Fig. 11(c)] and eventually form a single large cluster instead of a ring [Fig. 11(d)].

Unfortunately, this (quasi)linear change of the parameters into the microphase regime is not a universal solution that is guaranteed to result in a stable state if only the right initial temperature and transition time is picked. For instance, going from the fluid at $(B_i, T_i) = (0, T_c - 0.195$ K) to the cluster

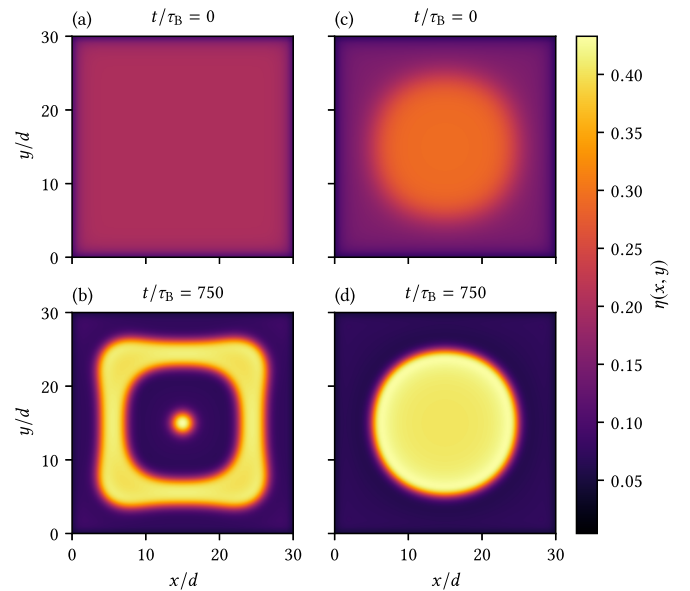


FIG. 11. Dynamic evolution of the density profile of a system with $L = 30d$ and $\eta^b = 0.19$. After equilibrating into a fluid state at $B = 0$ and $T = T_c - 0.20$ K (a) and then going quasilinearly to $B = 8.7 \mu\text{T}$ and $T = T_c - 0.16$ K during the period $[0, 1000 \tau_B]$, a ring with a central cluster eventually develops (b). When starting with $T = T_c - 0.19$ K instead (c), only a single large cluster forms (d).

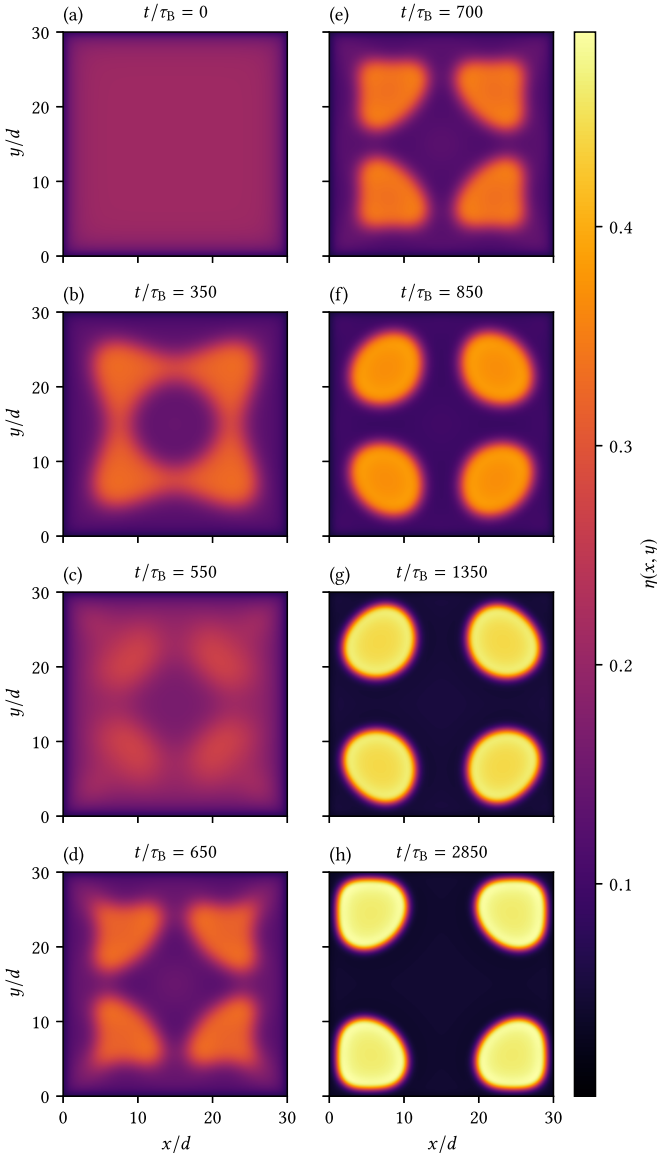


FIG. 12. Dynamic evolution of the density profile of a system with $L = 30d$ and $\eta^b = 0.19$ after equilibrating into a fluid state at $B = 0$ and $T = T_c - 0.195$ K (a), and then going to $B = 7.2 \mu\text{T}$ and $T = T_c - 0.16$ K during the period $[0, 1500 \tau_B]$ according to Eqs. (53) and (54) as shown in Fig. 13. After about $2850 \tau_B$, the system has practically reached the stable cluster configuration [cf. panel (h) and Fig. 3(b)]. See the Supplemental Material [48] for an animation.

state at $(B_f, T_f) = (7.2 \mu\text{T}, T_c - 0.16 \text{ K})$ over $\tau_t = 1000 \tau_B$ for $L = 30d$ and $\eta^b = 0.19$, does not produce four clusters as in Fig. 3(b), but a metastable ring instead. This does not come as a large surprise, however: Since the early-time dynamics are dominated by the temperature-dependent attraction, the evolution toward two final states with equal temperature and only slightly different magnetic fields (i.e., $B_f = 7.2 \mu\text{T}$ for the cluster vs. $B_f = 8.7 \mu\text{T}$ for the ring state) can be expected to be very similar in the beginning; and once a solid ring has developed in this stage, it becomes hard (if not impossible, even) to break it apart into clusters by increasing the repulsion.

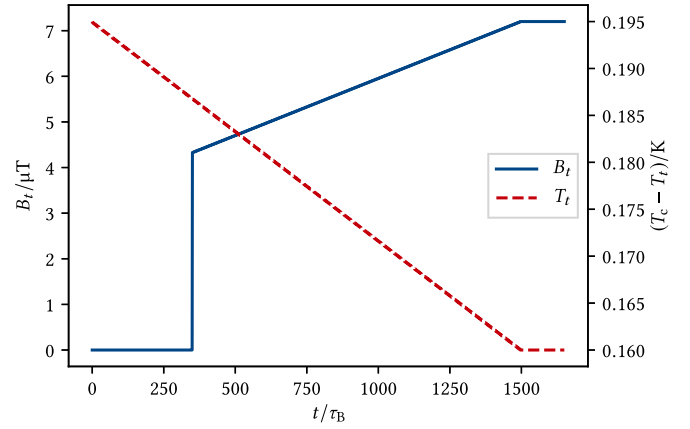


FIG. 13. Magnetic field B_t and temperature T_t as a function of time t during the dynamic evolution from the fluid to the cluster configuration for $L = 30d$ and $\eta^b = 0.19$ shown in Fig. 12.

Our findings so far suggest that the path taken through parameter space into the microphase regime has a larger influence on the dynamics and the ensuing structure of the system than the endpoint of that path itself, and that similar paths lead to similar states (which may very well only be metastable).

Devising a route from the fluid into the cluster phase proved rather challenging and took dozens of failed attempts until we finally came upon a strategy that seemed to work reliably. As before, the temperature is simply increased quasilinearly from T_i to T_f over a transition time τ_t with a step length of $\tau_s \ll \tau_t$,

$$T_t = \begin{cases} T_i & \text{for } t < 0, \\ T_i + (T_f - T_i) \frac{[t/\tau_s]}{\tau_t/\tau_s} & \text{for } 0 \leq t < \tau_t, \\ T_f & \text{otherwise.} \end{cases} \quad (53)$$

The magnetic field, however, first remains at B_i until some time $\tau_m \in (0, \tau_t)$, at which point it jumps instantaneously to an intermediate value $B_m \in (B_i, B_f)$ and then goes quasilinearly to B_f at time τ_t ,

$$B_t = \begin{cases} B_i & \text{for } t < \tau_m, \\ B_m + (B_f - B_m) \frac{[(t - \tau_m)/\tau_s]}{(\tau_t - \tau_m)/\tau_s} & \text{for } \tau_m \leq t < \tau_t, \\ B_f & \text{otherwise.} \end{cases} \quad (54)$$

Again, the correct choice of T_i , τ_t , B_m , and τ_m (we always use $B_i = 0$ for an initial fluid configuration) is crucial, but also not that difficult in the end, as we shall demonstrate. Figure 12 shows the evolution of the density profile for $L = 30d$ and $\eta^b = 0.19$ from $B_i = 0$ and $T_i = T_c - 0.195$ K to $B_f = 7.2 \mu\text{T}$ and $T_f = T_c - 0.16$ K using the method just described; the corresponding magnetic field and temperature as a function of time can be seen in Fig. 13. The transition time τ_t , and hence the rate of change of the temperature, needs to be chosen such that after some time, a ring forms that has four thick corners connected by very thin and short bridges [Fig. 12(b)]; for the current example, we settled on $\tau_t = 1500 \tau_B$. At one point, the corners of the ring are the most pronounced and the links between them the weakest; this is the moment τ_m when we turn the magnetic field up to B_m . For the present case, we chose $\tau_m = 350 \tau_B$ and $B_m = 0.6 B_f$. The sudden increase of the repulsion blows the ring apart and severs the

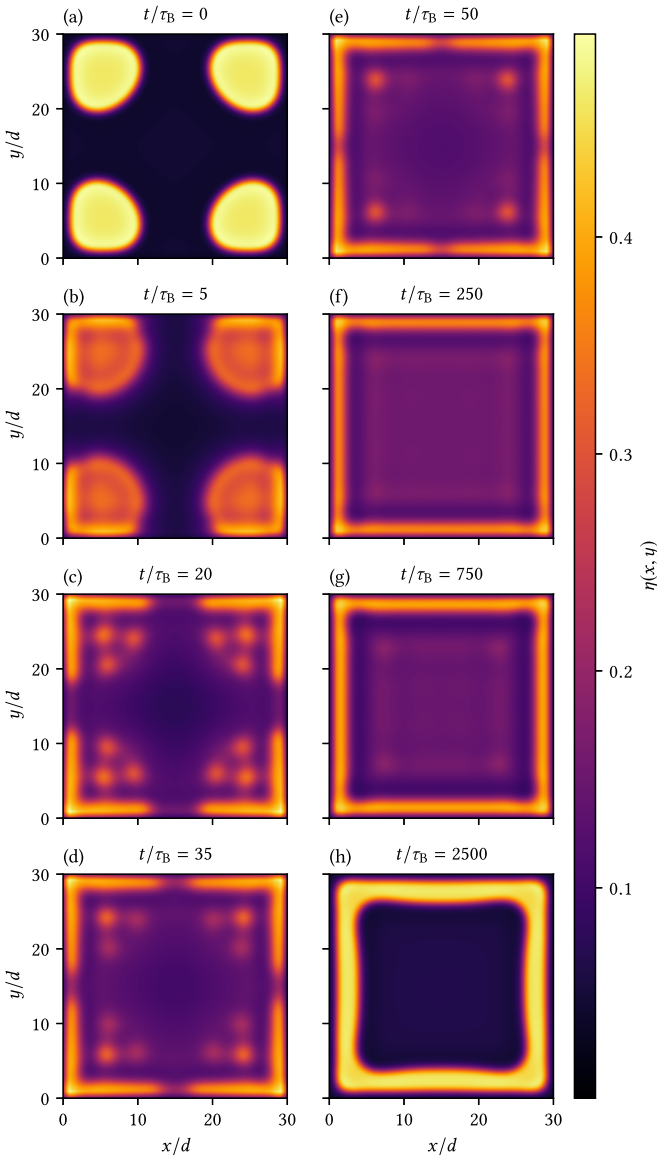


FIG. 14. Dynamic evolution of the density profile of a system with $L = 30d$, $\eta^b = 0.19$ and $T = T_c - 0.16$ K after equilibrating into a cluster state at $B = 7.2 \mu\text{T}$ [cf. panel (a) and Fig. 3(b)], and then going to $B = 8.7 \mu\text{T}$ during the period $[0, 2250 \tau_B]$ as shown in Fig. 15. After about $2500 \tau_B$, the system has practically reached the stable ring configuration [cf. panel (h) and Fig. 3(g)]. See the Supplemental Material [48] for an animation.

connections between its corners [Fig. 12(c)]. As the attraction gets stronger, the remains gather into four clusters [Figs. 12(d) and 12(e)] that become more distinct over time and repel each other [Figs. 12(f) and 12(g)] as they slowly reach their final position while the system approaches a stable equilibrium [cf. Figs. 12(h) and 3(b)].

Until now, we have only looked at the rather complicated dynamics from the fluid to the cluster or ring phase. The opposite direction turned out to be much simpler: Starting with a cluster or ring configuration, an instantaneous jump in parameter space into the fluid regime with $B = 0$ unsurprisingly always led to the dissolution of the structures and eventually resulted in a stable state.

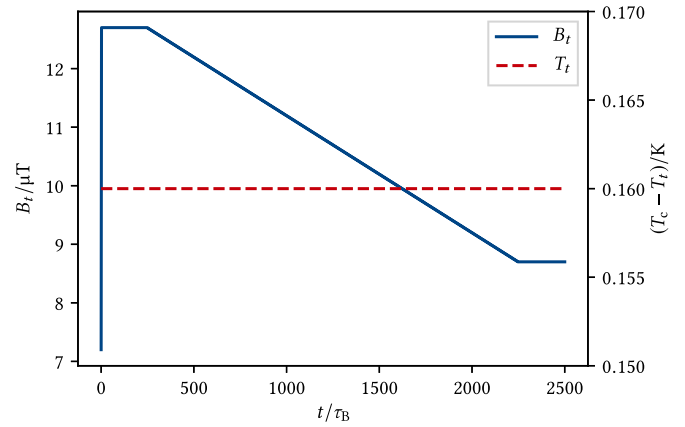


FIG. 15. Magnetic field B_t and temperature T_t as a function of time t during the dynamic evolution from the cluster to the ring configuration for $L = 30d$ and $\eta^b = 0.19$ shown in Fig. 14.

More interesting are transitions from the cluster to the ring phase, and vice versa. Recall that we found these two phases to overlap for $L = 30d$ and $T = T_c - 0.16$ K [Fig. 6(a)], which means that there exists both stable cluster and ring configurations for equal packing fractions but different magnetic fields. Examples for $\eta^b = 0.19$ are the previously targeted cluster state at $B = 7.2 \mu\text{T}$ [Fig. 3(b)] and the ring state at $B = 8.7 \mu\text{T}$ [Fig. 3(g)]. Our attempts to take the magnetic field directly from one value to the other, be it abruptly or (quasi)linearly, failed; either the clusters would recede further into the corners of the system or the ring would contract and shrink, but no phase transition could be observed. To destabilize and leave one phase, we first had to go beyond the magnetic field at which we actually wanted to end up. Figure 14 shows the dynamic evolution from the cluster to the ring state when the magnetic field is varied according to Fig. 15. By changing B from $7.2 \mu\text{T}$ to $12.7 \mu\text{T}$ at $t = 0$, the cluster are blown apart and the particles are subsequently pushed against the walls. After a thin ring has formed at $t = 250 \tau_B$, we quasilinearly dial B very slowly (otherwise, small clusters would develop inside the ring) down to $8.7 \mu\text{T}$ for $t/\tau_B \in [250, 2250]$. By approximately $t = 2500 \tau_B$, the density profile has basically converged to equilibrium [cf. Figs. 14(h) and 3(g)]. Unfortunately, we were unable to find a solution for the other way around, i.e., breaking a ring into four clusters by only manipulating the magnetic field; if B is brought too far below $7.2 \mu\text{T}$, then the tightening ring eventually just becomes one large cluster.

Let us last also take a brief look at the smaller system with $L = 20d$. The general behavior we observed proved to be more or less identical to the one for $L = 30d$. In particular, the same strategies could be used to go from a fluid to a cluster [Figs. 16(a)–16(d) and 17(a)] or ring [Figs. 16(e)–16(h) and 17(b)] configuration. Interestingly, however, the required transition times for $L = 20d$ ($\tau_t = 150 \tau_B$ into the cluster and $\tau_t = 100 \tau_B$ into the ring phase) are an order of magnitude shorter than those for $L = 30d$. It turns out that transition times can also be too long; for instance, using $\tau_t = 1000 \tau_B$ instead of $\tau_t = 100 \tau_B$ produces a single large cluster instead of a ring for $L = 20d$.

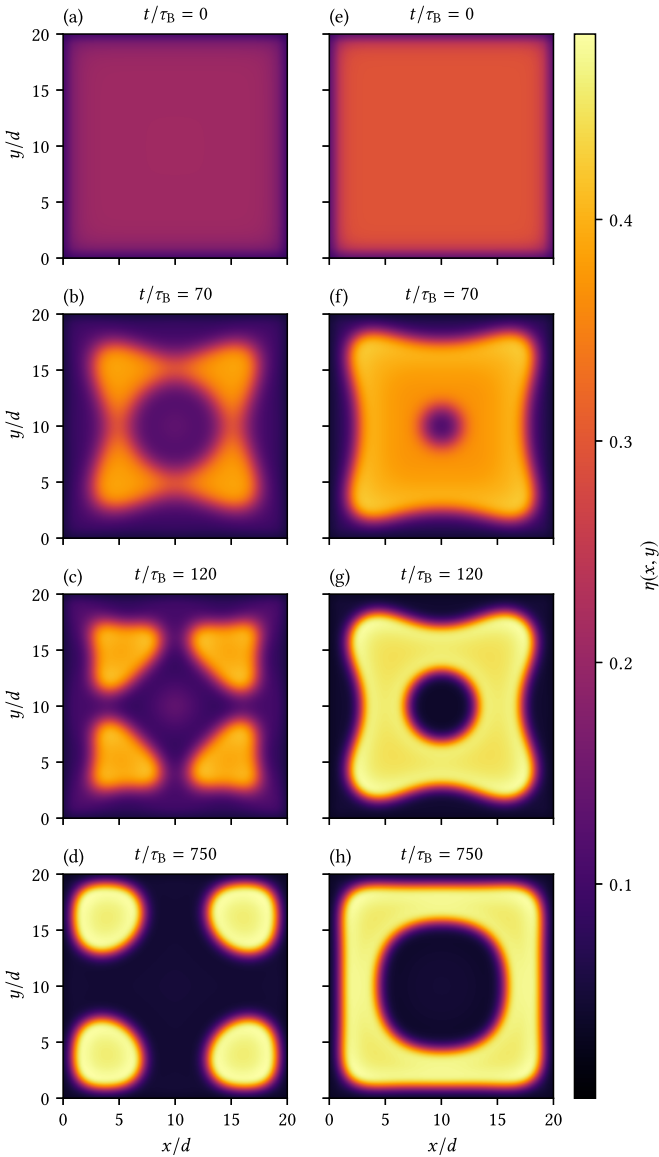


FIG. 16. *Left column*: Dynamic evolution of the density profile of a system with $L = 20d$ and $\eta^b = 0.19$ after equilibrating into a fluid state at $B = 0$ and $T = T_c - 0.2$ K (a), and then going to $B = 7.8 \mu\text{T}$ and $T = T_c - 0.16$ K according to Fig. 17(a) during the period $[0, 150 \tau_B]$. After about $750 \tau_B$, the system has practically reached the stable cluster configuration [cf. panel (d) and Fig. 4(a)]. *Right column*: The same scenario, but with $\eta^b = 0.27$ and the transition shown in Fig. 17(b) during $[0, 100 \tau_B]$. After about $750 \tau_B$, a stable ring has formed [cf. panel (h) and Fig. 4(b)]. See the Supplemental Material [48] for animations.

V. CONCLUSION

We have studied a finite two-dimensional colloidal system with attractive critical Casimir and repulsive magnetic dipole forces that can be tuned easily and independently from each other via the temperature and the strength of an external magnetic field, respectively.

Our analysis of the statics by means of density functional theory in square geometries with side lengths of 20 and 30 colloid diameters revealed evidence for microphase separa-

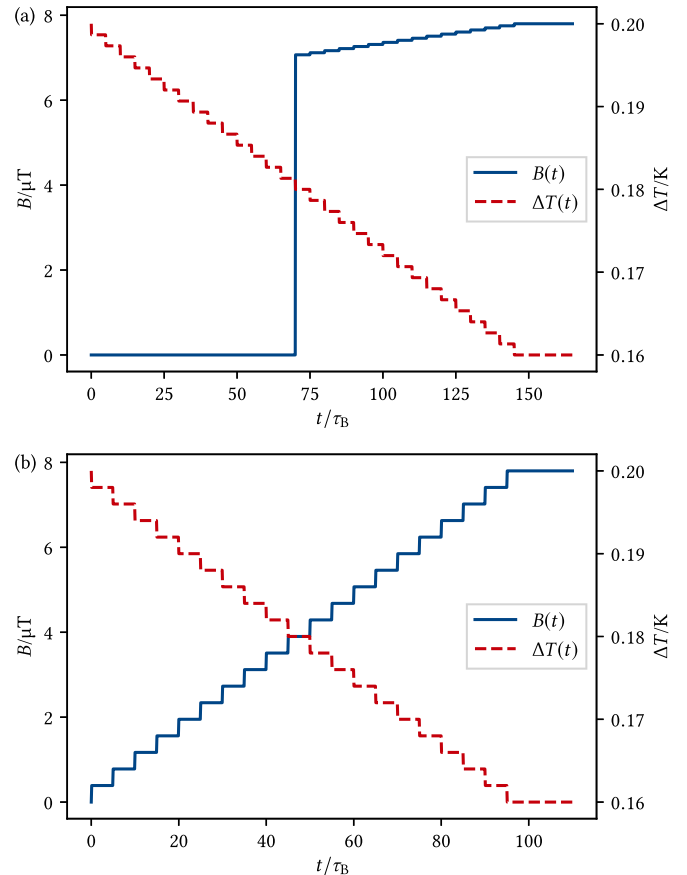


FIG. 17. *Top*: Magnetic field B_t and temperature T_t as a function of time t during the dynamic evolution from the fluid to the cluster configuration for $L = 20d$ and $\eta^b = 0.19$ shown in Figs. 16(a)–16(d). *Bottom*: The same, but for the dynamic evolution from the fluid to the ring configuration for $L = 20d$ and $\eta^b = 0.27$ shown in Figs. 16(e)–16(h).

tion. For certain temperatures and magnetic field strengths, we were able to identify four phases that alternately become stable as the bulk packing fraction is increased: A vapor, a cluster, a ring, and a liquid phase. The density distributions of the vapor and the liquid phase are almost uniform and thus rather unremarkable, whereas those of the cluster and ring phase display clear signs of the competing interactions between the particles: Due to a strong short-ranged attraction, the colloids form dense cluster or ring structures that are kept apart by a weak long-ranged repulsion. For a fixed temperature, we compiled phase diagrams that show which phases are stable for which combinations of the bulk packing fraction and the magnetic field. We noticed that the cluster phase is only stable for a relatively small range of bulk packing fractions and that it is separated from the vapor and ring phases by wide regions of coexistence. An interesting feature only present in the larger system is an overlap between the cluster and ring phases in the sense that for certain packing fractions, one can in principle transition from either phase to the other just by changing the magnetic field.

We then went on to investigate the dynamics of the system via dynamic density functional theory. Going from a fluid

configuration with only minimal attraction and no repulsion (by cooling the system further below the critical temperature and turning the magnetic field off) into the cluster or ring regime of the phase diagram by varying the temperature and the magnetic field over time, we tried to ascertain how the path taken through parameter space affects the outcome of the temporal evolution of the density profile. We found that a single instantaneous jump from the initial to the final parameters always resulted in metastable states with a multitude of smaller structures, a consequence of the development of many local aggregations due to the suddenly increased attraction. In fact, our research suggests that different strategies are necessary to generate different stable configurations. For the assembly of a ring, a linear change of the temperature and the magnetic field proved successful, provided that a suitable initial state and transition time are chosen. A slight modification, whereby the magnetic field at first remains disabled for a certain amount of time before it is abruptly turned on to some intermediate value and then increased linearly to its final strength, was

also able to produce a stable cluster configuration. These two methods worked for both the smaller and the larger system, but the latter required much slower transitions than the former. Where the two phases overlapped, we showed that it is even possible to go from a cluster to a ring state by only altering the magnetic field, but failed to discover a way to do so for the opposite direction.

Our findings demonstrate that it is highly nontrivial to produce a configuration with a specific structure in a system with competing interactions, even if it is thermodynamically stable. Carefully choosing a path into and inside the microphase regime turns out to be crucial; otherwise, the system is more likely than not to reach a metastable state, potentially with a highly irregular density profile. We suspect that this could be an important reason for the difficulty to observe stable and symmetric configurations in experiments, and would be very interested to see whether our proposed solutions work as well in practice as they do in theory.

-
- [1] M. Seul and D. Andelman, *Science* **267**, 476 (1995).
- [2] F. S. Bates and G. H. Fredrickson, *Annu. Rev. Phys. Chem.* **41**, 525 (1990).
- [3] A. K. Khandpur, S. Förster, F. S. Bates, I. W. Hamley, A. J. Ryan, W. Bras, K. Almdal, and K. Mortensen, *Macromolecules* **28**, 8796 (1995).
- [4] H. M. McConnell, L. K. Tamm, and R. M. Weis, *Proc. Natl. Acad. Sci. USA* **81**, 3249 (1984).
- [5] M. Lösche, J. Rabe, A. Fischer, B. Rucha, W. Knoll, and H. Möhwald, *Thin Solid Films* **117**, 269 (1984).
- [6] D. Andelman, F. Brochard, and J. Joanny, *J. Chem. Phys.* **86**, 3673 (1987).
- [7] N. G. Almarza, J. Pękalski, and A. Ciach, *J. Chem. Phys.* **140**, 164708 (2014).
- [8] Y. Zhuang, K. Zhang, and P. Charbonneau, *Phys. Rev. Lett.* **116**, 098301 (2016).
- [9] D. Pini and A. Parola, *Soft Matter* **13**, 9259 (2017).
- [10] A. Ciach, *Phys. Rev. E* **78**, 061505 (2008).
- [11] A. Ciach, J. Pękalski, and W. T. Gózdź, *Soft Matter* **9**, 6301 (2013).
- [12] A. J. Archer, *Phys. Rev. E* **78**, 031402 (2008).
- [13] C. P. Royall, *Soft Matter* **14**, 4020 (2018).
- [14] F. Ghezzi and J. C. Earnshaw, *J. Phys.: Condens. Matter* **9**, L517 (1997).
- [15] J. Ruiz-García, R. Gámez-Corrales, and B. I. Ivlev, *Phys. Rev. E* **58**, 660 (1998).
- [16] R. P. Sear, S.-W. Chung, G. Markovich, W. M. Gelbart, and J. R. Heath, *Phys. Rev. E* **59**, R6255(R) (1999).
- [17] C. A. Helm and H. Möhwald, *J. Phys. Chem.* **92**, 1262 (1988).
- [18] K. Marolt, M. Zimmermann, and R. Roth, *Phys. Rev. E* **100**, 052602 (2019).
- [19] O. Zvyagolskaya, A. J. Archer, and C. Bechinger, *Europhys. Lett.* **96**, 28005 (2011).
- [20] O. V. Zvyagolskaya, Critical Casimir effect in colloidal model systems, Ph.D. thesis, University of Stuttgart, 2012, <https://elib.uni-stuttgart.de/handle/11682/5082>.
- [21] R. Bubeck, C. Bechinger, S. Naser, and P. Leiderer, *Phys. Rev. Lett.* **82**, 3364 (1999).
- [22] S. H. Behrens and D. G. Grier, *J. Chem. Phys.* **115**, 6716 (2001).
- [23] C. Hertlein, L. Helden, A. Gambassi, S. Dietrich, and C. Bechinger, *Nature (London)* **451**, 172 (2008).
- [24] A. Gambassi, A. Maciołek, C. Hertlein, U. Nellen, L. Helden, C. Bechinger, and S. Dietrich, *Phys. Rev. E* **80**, 061143 (2009).
- [25] M. Krech, *Phys. Rev. E* **56**, 1642 (1997).
- [26] M. Krech, *J. Phys.: Condens. Matter* **11**, R391 (1999).
- [27] T. G. Mattos, L. Harnau, and S. Dietrich, *J. Chem. Phys.* **138**, 074704 (2013).
- [28] T. G. Mattos, L. Harnau, and S. Dietrich, *Phys. Rev. E* **91**, 042304 (2015).
- [29] A. Maciołek and S. Dietrich, *Rev. Mod. Phys.* **90**, 045001 (2018).
- [30] M. T. Dang, A. V. Verde, V. D. Nguyen, P. G. Bolhuis, and P. Schall, *J. Chem. Phys.* **139**, 094903 (2013).
- [31] S. Paladugu, A. Callegari, Y. Tuna, L. Barth, S. Dietrich, A. Gambassi, and G. Volpe, *Nat. Commun.* **7**, 11403 (2016).
- [32] K. Zahn, J. M. Méndez-Alcaraz, and G. Maret, *Phys. Rev. Lett.* **79**, 175 (1997).
- [33] R. Evans, *Adv. Phys.* **28**, 143 (1979).
- [34] J.-P. Hansen and I. R. McDonald, *Theory of Simple Liquids*, 4th ed. (Academic Press, San Diego, CA, 2013).
- [35] R. Roth, K. Mecke, and M. Oettel, *J. Chem. Phys.* **136**, 081101 (2012).
- [36] A. J. Archer, B. Chacko, and R. Evans, *J. Chem. Phys.* **147**, 034501 (2017).
- [37] D. Stopper and R. Roth, *J. Chem. Phys.* **147**, 064508 (2017).
- [38] A. Ciach, *Phys. Rev. E* **100**, 062607 (2019).
- [39] H. Serna, E. G. Noya, and W. T. Gózdź, *Soft Matter* **16**, 718 (2020).
- [40] J. Pękalski, E. Bildanau, and A. Ciach, *Soft Matter* **15**, 7715 (2019).
- [41] X. B. Xu, Z. H. Wang, X. N. Xu, G. Y. Fang, and M. Gu, *J. Chem. Phys.* **152**, 054906 (2020).

- [42] Y. H. Liu, L. Y. Chew, and M. Y. Yu, *Phys. Rev. E* **78**, 066405 (2008).
- [43] U. M. B. Marconi and P. Tarazona, *J. Chem. Phys.* **110**, 8032 (1999).
- [44] U. M. B. Marconi and P. Tarazona, *J. Phys.: Condens. Matter* **12**, A413 (2000).
- [45] A. J. Archer and M. Rauscher, *J. Phys. A: Math. Gen.* **37**, 9325 (2004).
- [46] S. M. Cox and P. C. Matthews, *J. Comput. Phys.* **176**, 430 (2002).
- [47] D. Stopper and R. Roth, *Phys. Rev. E* **97**, 062602 (2018).
- [48] See Supplemental Material at <http://link.aps.org/supplemental/10.1103/PhysRevE.102.042608> for animations of the dynamic evolution of the density profiles shown in Figs. 8, 9, 12, 14, and 16.